JACS
JOURNAL OF THE AMERICAN CHEMICAL SOCIETY

Article

pubs.acs.org/JACS

FeB_6 Monolayers: The Graphene-like Material with Hypercoordinate Transition Metal

Haijun Zhang,[†] Yafei Li,[‡] Jianhua Hou,[†] Kaixiong Tu,[†] and Zhongfang Chen*[,†]

[†]Department of Chemistry, Institute for Functional Nanomaterials, University of Puerto Rico, Rio Piedras Campus, San Juan, Puerto Rico 00931, United States

[‡]College of Chemistry and Materials Science, Jiangsu Key Laboratory of Biofunctional Materials, Nanjing Normal University, Nanjing, Jiangsu 210046, China

Supporting Information

ABSTRACT: By means of density functional theory (DFT) computations and global minimum search using particle-swarm optimization (PSO) method, we predicted three FeB_6 monolayers, namely α-FeB_6, β-FeB_6 and γ-FeB_6, which consist of the Fe©B_x (x = 6, 8) wheels with planar hypercoordinate Fe atoms locating at the center of six- or eight-membered boron rings. In particular, the α-FeB_6 sheet constructed by Fe©B_8 motifs is the global minimum due to completely shared and well delocalized electrons. The two-dimensional (2D) boron networks are dramatically stabilized by the electron transfer from Fe atoms, and the FeB_6 monolayers have pronounced stabilities. The α-FeB_6 monolayer is metallic, while the β-FeB_6 and γ-FeB_6 sheets are semiconductors with indirect band gaps and significant visible-light absorptions. Besides the novel chemical bonding, the high feasibility for experimental realization, and unique electronic and optical properties, render them very welcome new members to the graphene-like materials family.

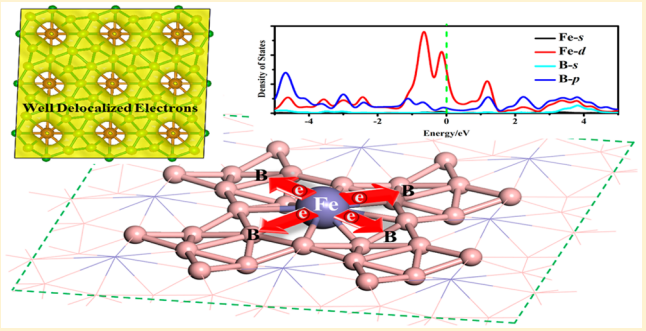

1. INTRODUCTION

Molecules with planar hypercoordinate carbon have greatly enriched the chemical bonding theory and provided many potential applications due to their exceptional structural, electronic, magnetic and optical properties.[1,2] Since Hoffmann, Alder, and Wilcox suggested strategies to stabilize planar tetracoordinate carbon (ptC),[3] and Schleyer et al. successfully computed the first planar ptC minimum with atypical geometries,[4] numerous ptCs have been described by the experimental and theoretical studies.[5−14] Moreover, molecules/clusters containing planar carbon with even higher coordination, such as penta-[15−19] and hexacoordination,[20−22] have also been achieved.

The concept of "planar hypercoordination chemistry" can be extended to other elements as well. Compounds with planar hypercoordination of other main group elements, such as boron,[23,24] nitrogen,[25,26] oxygen and sulfur,[27,28] silicon and germanium,[29] as well as phosphorus and arsenic,[30,31] have been theoretically and/or experimentally examined. Moreover, such unusual planar hypercoordinate configurations are also available for transition metals (TMs).[32] Schleyer and co-workers[33,34] theoretically predicted many neutral and charged molecules TM©B_n (n = 7−10), in which the central TM atom is at the center of the boron wheel. Notably several global minima with planar hypercoordinate motifs, such as Fe©B_8^{2-} (D_{8h}), Co©B_8^- (D_{8h}), and Fe©B_9^- (D_{9h}), were verified by the joint theoretical−experimental study of Wang and Boldyrev.[35] Subsequently, Wang and Boldyrev's joint efforts theoretically predicted, experimentally produced and detected even more planar hypercoordinate species, such as Ru©B_9^- (D_{9h}),[36] M©B_9^- (M = Rh, Ir) (D_{9h}),[37] and V©B_9^- (C_{2v}).[38] Amazingly, the highest coordination number of 10 was achieved in M©B_{10}^- (M = Ta, Nb) (D_{10h}).[39,40]

Interestingly, planar hypercoordinate carbon motifs can be extended to periodic systems. In 2004, by means of density functional theory (DFT) computations, Hoffmann and co-workers[41] proposed a potentially realizable three-dimensional networks of C_5Li_2 and C_5Zn, which are constructed by the ptC-containing C_5^{2-} building block. Ever since, other planar hypercoordinate carbon (phC) motifs have been extended to two-dimensional (2D) graphene-like materials with novel geometries and exceptional characteristics, such as B_xC_y,[42] TiC,[43] Al_xC,[44,45] and Be_2C.[46] Besides phCs, monolayers containing other elements in the planar hypercoordinate form, such as nonmetal-element silicon and germanium,[47] as well as metal-element silver, gold and platinum.[48]

In view of all these great achievements, a question arises naturally, is it possible to get (quasi)planar 2D materials featuring hypercoordinate transition metal motifs? To address this problem, in this work, we performed systematic DFT computations to search for 2D materials containing hyper-

Received: February 18, 2016
Published: April 1, 2016

DOI: 10.1021/jacs.6b01769
J. Am. Chem. Soc. 2016, 138, 5644−5651

coordinate transition metal atoms, and investigated the intrinsic electronic and optical properties. The electron deficient boron has been of our first choice to build up the 2D framework, since in clusters the boron rings can help obtain the planar hypercoordination of TMs.[32−40] We selected Fe as a representative of TM, since it is earth abundant and its planar hypercoordination was found in the Fe©B_6H_6 clusters.[49] Our computations identified three stable 2D sheets, namely α-FeB_6, β-FeB_6 and γ-FeB_6, in which each Fe atom coordinates with six or eight B atoms to form a (quasi-)planar hexa- or octacoordinate iron. The α-FeB_6 system containing the octacoordinate Fe atoms and close-packed boron atoms is the global minimum, owing to the electrons supplement for boron atoms and the well delocalized electrons in this Fe−B network. The α-FeB_6 monolayer is metallic, while the β-FeB_6 and γ-FeB_6 sheets are semiconductors with indirect band gaps and visible-light absorption. This is the first attempt to extend the planar hypercoordinate TMs into extended systems, which we hope can significantly promote the diversity of 2D materials with novel chemical bonding.

2. COMPUTATIONAL METHODS

Our DFT computations were performed using the Vienna ab initio simulation package (VASP).[50,51] The projector-augmented plane wave (PAW)[52] approach was used to represent the ion-electron interaction. The electron exchange-correlation functional was treated using generalized gradient approximation (GGA) in the form proposed by Perdew, Burke and Ernzerhof (PBE).[53] The energy cutoff of the plane wave was set to 600 eV with the energy precision of 10^{-6} eV. The atomic positions were fully relaxed until the maximum force on each atom was less than 10^{-4} eV/Å. The Brillouin zone was sampled with a 11 × 11 × 1 Γ-centered Monkhorst−Pack k-points grid for geometry optimization and self-consistent calculations.

To assess the kinetic stability of FeB_6 2D structures, phonon dispersion analysis was performed using the Phonopy code[54] interfaced with the density functional perturbation theory (DFPT)[55] as implemented in VASP. The ab initio molecular dynamics (AIMD) simulations using PAW method and PBE functional were carried out to evaluate the thermal stabilities of all the predicted FeB_6 monolayers. In the MD simulations, the initial configurations of FeB_6 monolayers with 3 × 3 supercell (9 Fe atoms and 54 B atoms) was annealed at different temperatures, each MD simulation in NVT ensemble lasted for 10 ps with a time step of 2.0 fs, and the temperature was controlled by using the Nosé−Hoover method.[56]

The particle-swarm optimization (PSO) method within the evolutionary algorithm, as implemented in CALYPSO code,[57] was employed to search for low-energy 2D FeB_6 monolayer sheets. As an unbiased global optimization method, PSO algorithm has successfully predicted highly stable structures of 2D boron−carbon sheets,[58] 2D boron sheets,[59,60] Be_2C monolayer,[46] as well as planar hexacoordinate Cu_2Si monolayer.[48] In our PSO calculations, the population size is set to 50, and the number of generation was maintained at 30. Unit cells containing total atoms of 7, 14, and 28 were considered. The required structure relaxations were performed by using PBE functional, as implemented in VASP code. Three stable FeB_6 monolayers, namely α-FeB_6, β-FeB_6 and γ-FeB_6 (Figure 1) were obtained. We placed the 2D FeB_6 monolayer in the xy plane with the z direction perpendicular to the layer plane, and a vacuum space of 15 Å in the z direction was adopted to avoid interactions between adjacent layers.

Note that the standard GGA tends to underestimate the band gaps, thus we adopted the Heyd−Scuseria−Ernzerhof (HSE06)[61] hybrid functional, which was proven to be a reliable method for the calculation of electronic and optical properties,[62] to calculate the band structures of all the FeB_6 systems. Due to their different crystal symmetries, the band structure of α-FeB_6 was computed along the special lines of Γ (0, 0, 0) → M (0.5, 0.5, 0) → X (0, 0.5, 0) → Γ (0, 0, 0), while those of β-FeB_6 and γ-FeB_6 were computed along the special lines connecting the following high-symmetry points, Γ (0, 0, 0), M (0.5, 0, 0), K (1/3, 1/3, 0) and Γ (0, 0, 0) in the k-space.

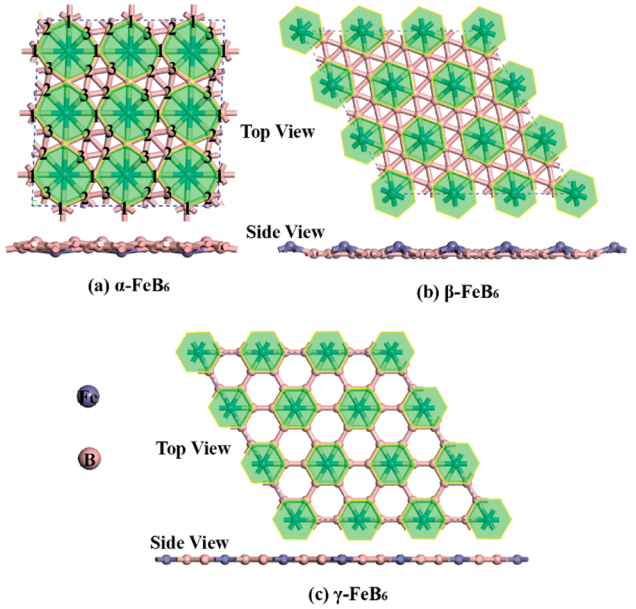

Figure 1. Optimized geometries of α-FeB_6, β-FeB_6 and γ-FeB_6 monolayers. Green-filled octagons and hexagons are guidelines for Fe©B_8 and Fe©B_6 wheels, respectively.

We also investigated the optical absorption properties of the semiconducting β-FeB_6 and γ-FeB_6 monolayers by calculating the complex dielectric constants (ε) at a given frequency using HSE hybrid functional with 21 × 21 × 1 k-point mesh. The dielectric constants can be defined as $\varepsilon(\omega) = \varepsilon_1(\omega) + i\varepsilon_2(\omega)$. After the obtainment of the real and imaginary part of ε, we can calculate the absorption coefficient $I(\omega)$ as given equation:[63]

$$I(\omega) = \sqrt{2}\,\omega\left[\sqrt{\varepsilon_1(\omega)^2 + \varepsilon_2(\omega)^2} - \varepsilon_1(\omega)\right]^{1/2} \quad (1)$$

As presented in the expression, only if the imaginary part $\varepsilon_2(\omega) > 0$, the absorption coefficient $I(\omega)$ will be above zero. Therefore, positive value of $\varepsilon_2(\omega)$ reflects the light absorption at a given frequency ω. The imaginary part is determined by a summation over empty states using the following expression:[64]

$$\varepsilon^{(2)}_{\alpha\beta}(\omega) = \frac{4\pi^2 e^2}{\Omega}\lim_{q\to 0}\frac{1}{q^2}\sum_{c,v,\vec{k}} 2w_{\vec{k}}\,\delta(\varepsilon_{c\vec{k}} - \varepsilon_{v\vec{k}} - \omega) \times \langle u_{c\vec{k}+e_\alpha\vec{q}}|u_{v\vec{k}}\rangle \langle u_{c\vec{k}+e_\beta\vec{q}}|u_{v\vec{k}}\rangle^* \quad (2)$$

3. RESULTS AND DISCUSSION

3.1. Geometric Structures of α-FeB_6, β-FeB_6 and γ-FeB_6 Monolayers. The ground state structures of FeB_6 were obtained through a comprehensive PSO search, which was followed by the full relaxation of random structures with VASP code. These computations led to three stable structures, which were named as α-FeB_6, β-FeB_6 and γ-FeB_6 (Figure 1), in the order of increasing energy.

Generally, all these FeB_6 monolayers are constructed by motifs of Fe-centered boron rings, in which the Fe atoms octacoordinate (hexacoordinate) with eight (six) boron atoms around them. In the γ-FeB_6 sheet, isolated Fe©B_6 wheels, which can be regarded as the dehydrogenated Fe©B_6H_6 clusters, are extended to a completely planar structure in a periodic arrangement (Figure 1c). Similar to the γ-FeB_6 sheet, the β-FeB_6 monolayer is also composed of Fe©B_6 wheels.

DOI: 10.1021/jacs.6b01769
J. Am. Chem. Soc. 2016, 138, 5644−5651

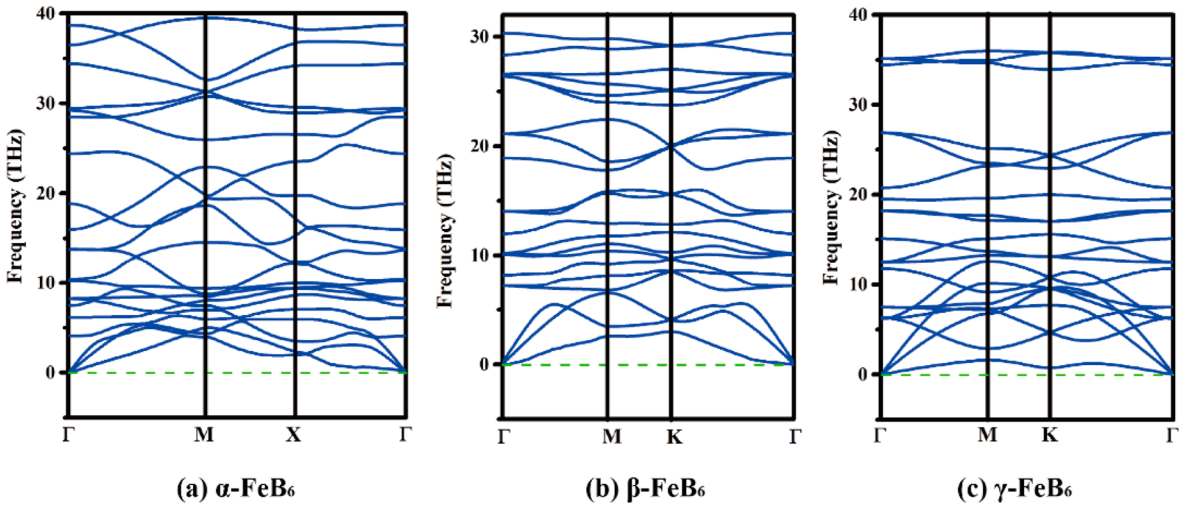

Figure 2. Phonon dispersion of the fully optimized FeB_6 monolayers in different geometries.

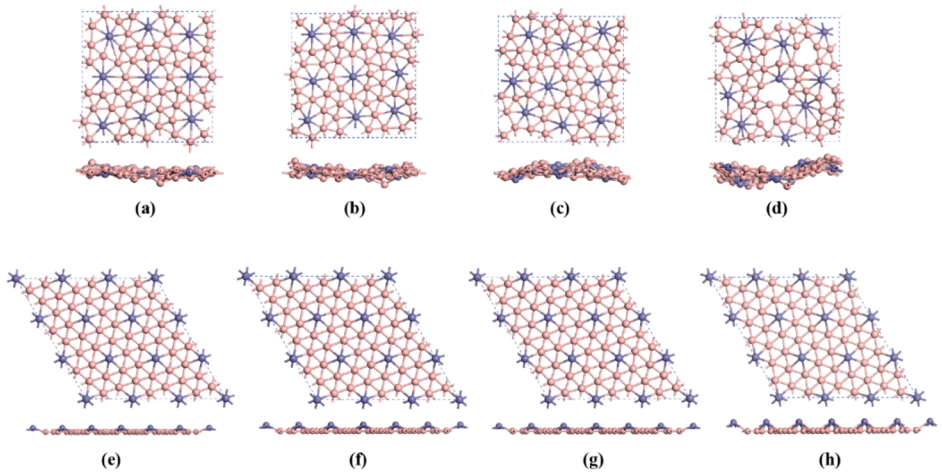

Figure 3. Snapshots of the (a, b, c,d) α-FeB_6 and (e, f, g, h) β-FeB_6 equilibrium structures at (a, e) 500 K, (b, f) 1000 K, (c, g) 1500 K and (d, h) 2000 K at the end of 10 ps AIMD simulations.

However, in the β-FeB_6, the Fe©B_6 units are not completely isolated, their boron edges are adjacently connected to each other (Figure 1b). The B atoms in β-FeB_6 and γ-FeB_6 sheets are hexacoordinate and tetracoordinate, respectively. In the energetically most favorable α-FeB_6 monolayer, the Fe©B_8 units are adjacent to each other and share four boron atoms with their four neighbors. Interestingly, the α-FeB_6 monolayer does not adopt the perfect tetragonal lattice, but prefers a slightly distorted configuration in which one lattice angle within the x–y plane is 88.1° (90.0° in the perfect tetragonal lattice), probably due to the Jahn–Teller effect.[37] For simplicity, the boron atoms within Fe©B_8 units are denoted by B1, B2 and B3, according to their different positions and coordination (Figure 1a). Both the B1 and B2 have six coordination, while the B3 atoms are pentacoordinate. Unlike the completely planar sheet of γ-FeB_6, the α-FeB_6 and β-FeB_6 sheets have quasi-planar 2D geometries, which may result from the extremely high density of Fe and B atoms. The buckled geometries of α-FeB_6 and β-FeB_6 sheets could help avoid the repulsive interaction between high-density iron and boron atoms, and thus, lead to the decrease of their total energies.

3.2. Thermodynamic, Kinetic and Thermal Stabilities of FeB_6 Monolayers. To access the experimental feasibility of the newly predicted FeB_6 monolayers, we first evaluated their thermodynamic stabilities by calculating their cohesive energies, $E_{coh} = (xE_{Fe} + 6xE_B - xE_{FeB6})/7x$, where E_{Fe}, E_B and E_{FeB6} are the total energies of a single Fe atom, a single B atom, and one unit cell of the FeB_6 monolayer, respectively. The computed cohesive energies of α-FeB_6, β-FeB_6 and γ-FeB_6 monolayers (5.79, 5.75, and 5.56 eV/atom, respectively) are higher than those of Be_2C (4.86 eV/atom),[46] Cu_2Si (3.46 eV/atom),[48] and Al_xC_y (3.97–5.17 eV/atom)[44,45] monolayers at the same theoretical level. The relatively large cohesive energies of these new 2D FeB_6 compounds suggest that the monolayers are stable phases of Fe–B systems. Moreover, according to the relative value of E_{coh}, the α-FeB_6 monolayer is energetically most preferable among these different phases of 2D FeB_6 systems.

Then, we evaluated the dynamical stabilities of FeB_6 monolayers by computing the phonon dispersion along the high-symmetry lines in first Brillouin zone (Figure 2). There is not any appreciable imaginary frequency in the phonon spectra of these FeB_6 monolayers, suggesting the kinetic stabilities of these different phases. The highest frequencies of α-FeB_6, β-FeB_6 and γ-FeB_6 sheets reach up to 1316 cm^{-1} (= 39.47 THz), 1011 cm^{-1} (30.31 THz) and 1200 cm^{-1} (35.98 THz),

DOI: 10.1021/jacs.6b01769
J. Am. Chem. Soc. 2016, 138, 5644–5651

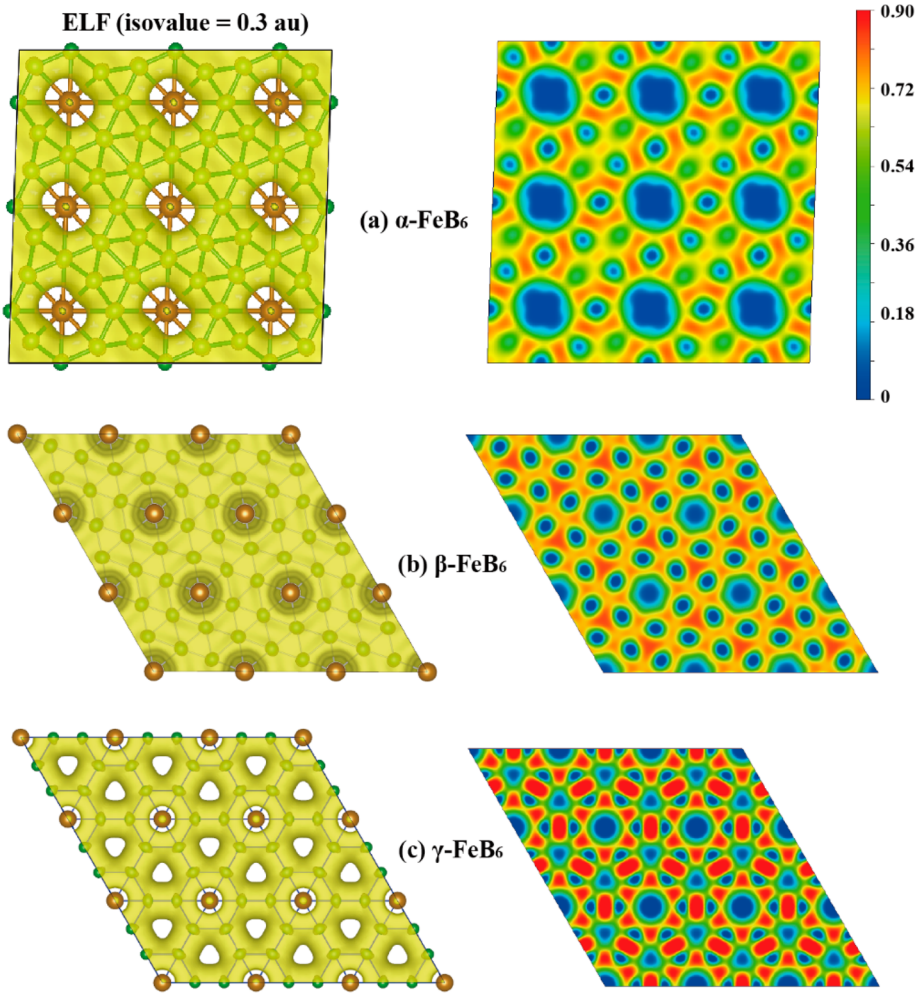

Figure 4. Isosurfaces of electron localization function (left) plotted with the value of 0.3 au and ELF maps (right) sliced perpendicular to (001) direction for (a) α-FeB_6, (b) β-FeB_6 and (c) γ-FeB_6 monolayers. In the ELF maps, the color of red and blue refer to the highest (0.90) and lowest value (0.00) of ELF, indicating accumulation and depletion of electrons at different colored regions, respectively.

respectively, which are higher than the highest frequencies of t-TiC sheet (810 cm^{-1}),[43] Cu_2Si (420 cm^{-1})[48] and MoS_2 monolayer (473 cm^{-1}).[65] These high-value frequencies in phonon spectra also indicate the robust Fe−B and B−B interactions in these newly predicted FeB_6 monolayers.

We further performed AIMD simulations to evaluate the thermal stabilities of FeB_6 monolayers. We used relatively large 3 × 3 supercell and carried out AIMD simulations at the temperatures of 500 K, 1000 K, 1500 K and 2000 K for α-FeB_6 and β-FeB_6 sheets, and at 300, 500, and 1000 K for γ-FeB_6 monolayer.

Snapshots of α-FeB_6 and β-FeB_6 sheets taken at the end of 10 ps simulations are presented in Figure 3. The framework of α-FeB_6 sheet is well kept in its original configuration with adjacently connected Fe©B_8 wheels at the temperature of 1000 K after 10 ps simulation, and does not evidently disrupt throughout a 10 ps dynamical simulation up to 1500 K (Figure 3a−c). However, at the extremely high temperature of 2000 K, the Fe©B_8 wheels are disrupted, and the hollow boron rings appear in the FeB_6 sheet (Figure 3d). Note that this does not mean that its melting point is between 1500 and 2000 K, but indicates that the α-FeB_6 should have enough kinetic energy to cross the barrier and turn to be corrupt at the temperatures between 1500 and 2000 K in a 10 *ps* time frame.[66] For β-FeB_6 sheet, the Fe−B framework is well kept in its hexagonal structure at a very high temperature of 2000 K after 10 ps simulation (Figure 3e-h), even at an extremely higher temperature of 3000 K (Figure S1). The well maintained geometries at such high temperatures, up to 1500 or 2000 K, indicate the high thermal stability of the α-FeB_6 and β-FeB_6 monolayer, respectively, and their possible applications at an extremely high temperature.

For the γ-FeB_6 sheet, the hexagonal geometry with isolated distribution of Fe©B_6 wheels is well retained at 300 K, as well as at mild thermal environment of 500 K, which suggest their thermal stability at nonextreme temperatures (Figure S2a,b). However, the γ-FeB_6 sheets collapsed after 10 ps simulations at 1000 K, implying it should have enough kinetic energy to get across the barrier in 10 ps between 500 and 1000 K (Figure S2c). Unlike the closely arranged Fe©B_6 wheels and triangular boron frameworks in β-FeB_6 sheet, the γ-FeB_6 has isolated Fe©B_6 wheels and nonexistence of triangular boron rings, which may lead to its thermodynamic instability at extremely high temperature.

Moreover, we examined the possibility of exfoliating the FeB_6 monolayers from their corresponding bulk phase by evaluating the interaction strength between two FeB_6 single layers. Three stacking patterns, namely the AA, AB and AC stacking, were

DOI: 10.1021/jacs.6b01769
J. Am. Chem. Soc. 2016, 138, 5644−5651

considered (Figure S3–S5). The geometric structures for double-layer FeB_6 systems were fully optimized with considering the van der Waals (vdW) interactions (at the PBE+D2 level of theory with Grimme vdW corrections[67]). Table S1 summarizes the interlayer distances and binding energies of these FeB_6 bilayers. Most of the interlayer distances are around 3.00 Å, which are comparable to the interlayer separation of graphite (3.34 Å)[68] and graphene/h-BN hybrid system (3.02).[69] Moreover, all these FeB_6 bilayers have smaller binding energies (14–102 meV) than those of graphene/BN hybrid systems (168–207 meV).[68] These computed interlayer distances and binding energies suggest that the newly predicted FeB_6 monolayers are stacked by rather weak vdW interactions, and have great probabilities to be physically/chemically exfoliated from their bulk phase.

3.3. Chemical Bonding and Stabilization Mechanism. To gain a deep insight into the unique bonding nature and stabilizing mechanism in these 2D materials, we analyzed the electron localization function (ELF).[70] The ELF is a useful tool for chemical bond classification, which can provide good descriptions of electron localization in molecules and solids. The jellium-like homogeneous electron gas can be presented by the ELF, which is renormalized to the values between 0.00 and 1.00. Generally, the values of 1.00 and 0.50 denotes the fully localized and fully delocalized electrons, respectively, while the value near 0.00 refers to very low charge density.[71] To highlight the in-plane multicentered bonds between B and B, as well as Fe and B atoms, we plotted the isosurfaces of ELFs for the α-FeB_6, β-FeB_6 and γ-FeB_6 sheets with the iso-value of 0.30 au. The ELF values at different regions can be visualized by different colors in ELF maps (Figure 4).

For α-FeB_6 and β-FeB_6 sheets, the electrons are well delocalized around the Fe atoms, and homogeneous electron gas is widely distributed in the boron frameworks, which can be proven by their ELF maps (Figure 4a,b). Except for the blue region around the Fe atoms, the whole boron frameworks are in the color corresponding to the values around 0.50, implying fully delocalized electrons in the boron networks of the α-FeB_6 and β-FeB_6 monolayers. The complete delocalization of electrons should lead to robust connection between the boron atoms, which is crucial to electronically stabilize these 2D Fe–B networks. Moreover, blue color around the Fe atom, corresponding to the ELF value of 0.00, suggests electron deficiency of Fe atoms in these 2D FeB_6 monolayers. Accordingly, there are remarkable electron transfers from Fe atoms to B frameworks in all these 2D FeB_6 systems. Hirshfeld charge analysis shows that each Fe atom in α-FeB_6 transfers 0.075 *e* to the adjacent B atoms, which denotes the considerable ionization of Fe atoms and electron supplement for boron frameworks in α-FeB_6 sheet. Similarly, boron atoms capture 0.016 *e* from each Fe atom in the β-FeB_6 sheet, also suggesting the electron supplement for boron atoms. This electron transfer leads to electron supplement for boron frameworks, and accordingly, stabilization of the iron boride systems.

For the γ-FeB_6 monolayer, unlike the completely shared and well delocalized electrons in α-FeB_6 and β-FeB_6 sheets, most electrons are localized at the isolated Fe©B_6 wheels (Figure 4c, Figure S6c). The electrons also accumulate at the region between edge-position boron atoms of neighboring Fe©B_6 wheels, suggesting the two-center two-electron B–B σ bonds in γ-FeB_6 system. Accordingly, the isolated Fe©B_6 motifs are only connected by the σ bonding between boron atoms, and most of electrons localize at the Fe©B_6 units. The lack of multicenter B–B bonds between Fe©B_6 units may explain its lower stability compared to the α- and β-phases.

The deformation electronic density (DED), which is defined as the total electron density of a FeB_6 monolayer subtracted by electron densities of isolated Fe and B atoms within the corresponding 2D crystal, is also calculated to verify their chemical bonding characteristics (Figure S6). The results of DED and ELF agree well with each other and have similar description of the electron distribution for each FeB_6 system.

We further explored the chemical bonding pattern of FeB_6 monolayers by employing the recently developed solid state Adaptive Natural Density Partitioning (SSAdNDP) method.[72] According to our computations, one unit cell of α-FeB_6 monolayer contains eight three-center-two-electron (3c-2e) B–Fe–B σ bonds, four 3c-2e B–B–B bonds, and one 9c-2e π bond over FeB_8 moiety (Figure S8), accounting for 26 electrons per unit cell. For β-FeB_6 monolayer (Figure S9), there are six 3c-2e B–Fe–B σ bonds, two 3c-2e B–B–B σ bonds, three 4c-2e B–B–B–B bonds, and two 7c-2e π bonds over FeB_6 moiety in one unit cell. For α-FeB_6 and β-FeB_6 monolayers, there are no classic 2c-2e bonds. In contrast, in γ-FeB_6 monolayer, the FeB_6 moieties are connected through the B–B single bonds. For one unit of FeB_6 monolayer (Figure S10), there are an unbound lone pair electrons on the Fe atom, three 2c-2e B–B bonds, six 3c-2e B–Fe–B bonds, and three 7c–2e π bonds over FeB_6 moiety. Thus, the abundance of multicenter bonds contributes significantly to the high stability of α- and β-phases, while the availability of more π bonds in γ-FeB_6 monolayer could contribute to its higher planarity.

3.4. Electronic Structures and Optical Properties. With such interesting chemical bonding, will these FeB_6 sheets possess novel properties? To address this question, we calculated the band structures, density of states (DOS), and optical absorptions of these FeB_6 monolayers.

In the band structure of α-FeB_6 sheet (Figure 5a), there are two band lines across the Fermi level. Thus, the α-FeB_6 monolayer is metallic. The high peaks of DOS around the Fermi level, which are predominately composed of Fe-*d* states, indicate the high density of carriers at Fermi level. These high density of electron states around the Fermi level suggest the available electrons that can participate the electronic transport, and accordingly, outstanding electric conductivity of the α-FeB_6 monolayer. The concomitant electric conductivity is in line with good electron delocalization as revealed by ELF and DED analyses

The β-FeB_6 and γ-FeB_6 are semiconductors, and have indirect band gaps of 0.50 and 1.27 eV, respectively (Figure 5b and 5c). The indirect band gaps should be beneficial to the restraint of electron–hole recombination in the photoelectric process, such as the photocatalytic reaction[73,74] and photovoltaic effect.[62] The projected DOS (PDOS) analysis shows that both the valence band maximum (VBM) and conduction band minimum (CBM) of β-FeB_6 monolayer are mainly contributed by *d* orbitals of Fe atoms. In the γ-FeB_6, the VBM is predominantly composed of B-*p* states at K point, while the CBM consists of slightly hybridized Fe-*d* and B-*p* states at the M point. The same conclusion can be obtained by analyzing the spatial charge distribution of VBMs and CBMs at the Γ point (Figure S7).

The band structures of β-FeB_6 and γ-FeB_6 semiconductors suggest their potential applications in visible-light solar harvesting/utilizing techniques or other narrow-gap-semiconductor equipment. Thus, we further explored the optical

DOI: 10.1021/jacs.6b01769
J. Am. Chem. Soc. 2016, 138, 5644–5651

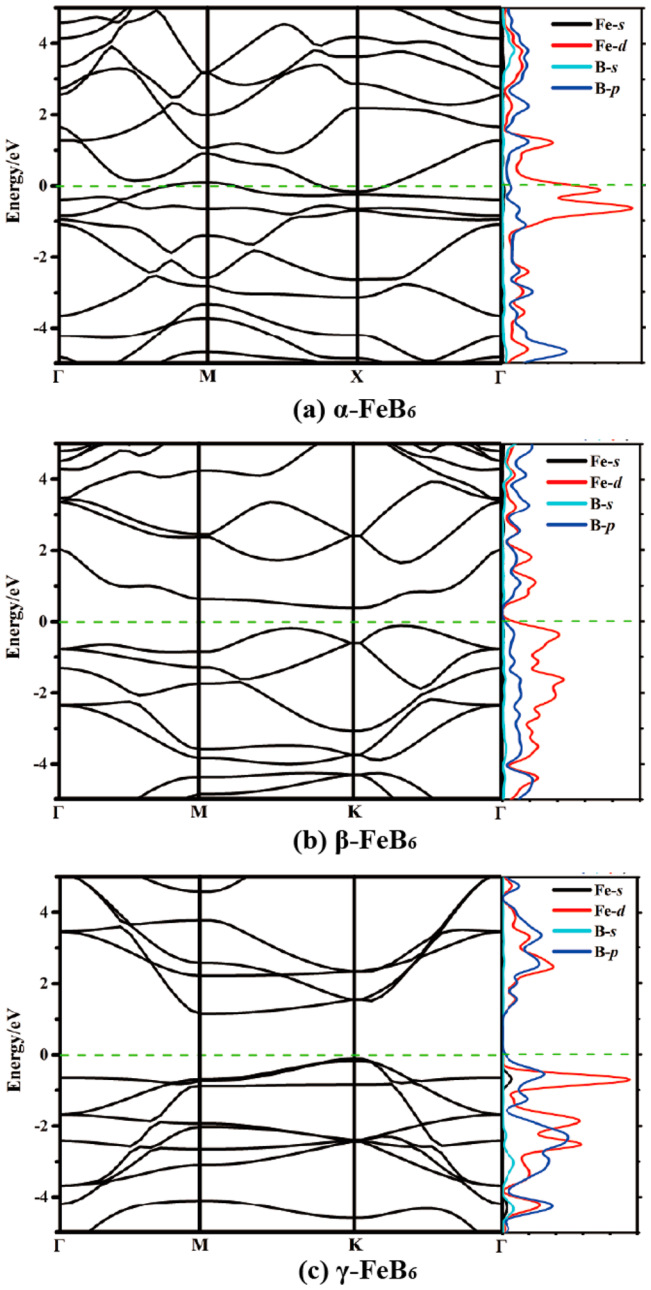

Figure 5. Band structures and projected DOS of (a) α-FeB_6, (b) β-FeB_6 and (c) γ-FeB_6 monolayers, calculated by HSE06 functional. Green dashed lines represent Fermi level at 0 eV.

absorption properties by calculating the complex dielectric constants $\varepsilon(\omega) = \varepsilon_1(\omega) + i\varepsilon_2(\omega)$ at a given frequency using HSE06 hybrid functional. As shown in Figure 6, there are obvious absorption peaks at 0.73 and 1.89 eV for the β-FeB_6 and γ-FeB_6 monolayers, respectively, resulting in visible-light absorption of these 2D FeB_6 sheets. Moreover, the high peaks of the imaginary part $\varepsilon_2(\omega)$ and the large area under the red curve at visible-light region (<3.0 eV) should result in high absorption coefficients at these frequencies, and thus high-efficiency visible absorption (<414 nm) of the β-FeB_6 and γ-FeB_6 monolayers. Accordingly, these newly predicted 2D materials may be practically utilized in visible-light driven photocatalysis, high-efficiency solar harvesting process, or other light-emitting devices.

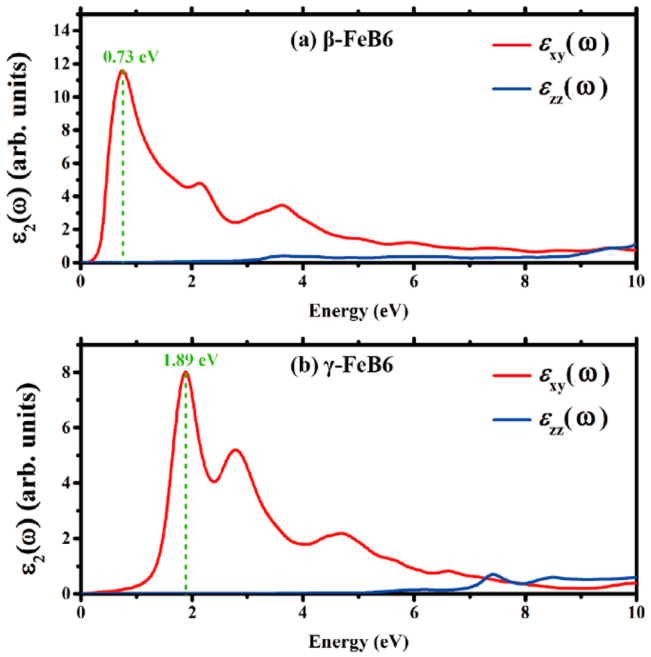

Figure 6. Imaginary parts of dielectric constants for (a) β-FeB_6 and (b) γ-FeB_6 sheets, respectively.

4. CONCLUSION

We performed comprehensive DFT computations to check the possibility to obtain graphene-like materials containing planar hypercoordinate transition metal atoms. Our computations identified three 2D FeB_6 monolayers, namely α-FeB_6, β-FeB_6 and γ-FeB_6, which process planar hypercoordinated Fe atoms and differently arranged boron atoms. Due to the electron transfer from Fe to B atoms, the 2D boron networks are dramatically stabilized to combine with Fe atoms and to form FeB_6 monolayers constructed by Fe©B_8 or Fe©B_6 motifs. All these three monolayers have sound thermodynamic, kinetic and thermal stabilities. Especially, as the global minimum, the α-FeB_6 sheet consisting of Fe©B_8 motifs, has the highest feasibility for experimental realization. The newly predicted α-FeB_6 sheet is a metallic material with high conductivity, due to the high density of electronic states around the Fermi level. Meanwhile, the β-FeB_6 and γ-FeB_6 sheets are semiconductors with indirect band gaps and significant visible-light absorptions, thus promising as high-efficiency photocatalysis, solar harvesting, or other luminescent devices.

Note that it is the first attempt to design graphene-like materials containing planar hypercoordinate transition metal atoms. Many more 2D materials with such unique chemical bonding may be identified shortly, especially 2D boron sheets containing transition metal atoms that can form planar hypercoordination with boron rings.[32] So far, the fabrication of boron monolayer is still very challenging in experiments, which may be due to the electron deficiency of boron atoms.[75,76] It is until very recently that Mannix et al. successfully synthesized the atomically thin 2D boron sheet (i.e., borophene) on silver surfaces under ultrahigh-vacuum conditions.[77] The electron transfer from the central metal atom to the surrounding boron framework may provide another strategy to stabilize planar boron nanosheets.

Our results not only extend the planar hypercoordinate transition metal concept into 2D systems, but also provide a promising strategy to stabilize the 2D boron networks and to

DOI: 10.1021/jacs.6b01769
J. Am. Chem. Soc. 2016, 138, 5644−5651

design boron related 2D materials, which could greatly enrich the diversity and advance the applications of graphene-like materials.

■ ASSOCIATED CONTENT

Supporting Information

The Supporting Information is available free of charge on the ACS Publications website at DOI: 10.1021/jacs.6b01769.

Snapshot of final β-FeB_6 sheet at 3000 K after 10 ps AIMD simulations; Snapshot of final γ-FeB_6 monolayers at 300 K, 500 and 1000 K, at the end of 10 ps AIMD simulations; The optimized structures of the α-FeB_6, β-FeB_6 and γ-FeB6 bilayer systems with different stacking patterns; Deformation electronic density for α-, β- and γ-FeB_6 monolayers; Charge distributions of valence band maximum and conduction band minimum at Γ point for the semiconducting β- and γ-FeB_6 monolayers; The SSAdNDP analysis of chemical bonding; The interlayer distances and binding energies of the bilayer FeB_6 systems. (PDF)

■ AUTHOR INFORMATION

Corresponding Author

*zhongfangchen@gmail.com

Notes

The authors declare no competing financial interest.

■ ACKNOWLEDGMENTS

This work was supported by NSF (Grant EPS-1002410) and Department of Defense (Grant W911NF-12-1-0083).

■ DEDICATION

This paper is dedicated to the 60th birthday of Professor Shengbai Zhang.

■ REFERENCES

(1) Yang, L. M.; Ganz, E.; Chen, Z. F.; Wang, Z. X.; Schleyer, P. v. R. *Angew. Chem., Int. Ed.* **2015**, *54*, 9468−9501.
(2) Keese, R. *Chem. Rev.* **2006**, *106*, 4787−4808.
(3) Hoffmann, R.; Alder, R. W.; Wilcox, C. F. *J. Am. Chem. Soc.* **1970**, *92*, 4992−4993.
(4) Collins, J. B.; Dill, J. D.; Jemmis, E. D.; Apeloig, Y.; Schleyer, P. v. R.; Seeger, R.; Pople, J. A. *J. Am. Chem. Soc.* **1976**, *98*, 5419−5427.
(5) Röttger, D.; Erker, G. *Angew. Chem., Int. Ed. Engl.* **1997**, *36*, 812−827.
(6) Erker, G. *Chem. Soc. Rev.* **1999**, *28*, 307−314.
(7) Siebert, W.; Gunale, A. *Chem. Soc. Rev.* **1999**, *28*, 367−371.
(8) Li, X.; Wang, L. S.; Boldyrev, A. I.; Simons, J. *J. Am. Chem. Soc.* **1999**, *121*, 6033−6038.
(9) Li, X.; Zhang, H. F.; Wang, L. S.; Geske, G. D.; Boldyrev, A. I. *Angew. Chem., Int. Ed.* **2000**, *39*, 3630−3632.
(10) Merino, G.; Méndez-Rojas, M. A.; Vela, A.; Thomas, H. *J. Comput. Chem.* **2007**, *28*, 362−372.
(11) Cui, Z. H.; Ding, Y. H.; Cabellos, J. L.; Osorio, E.; Islas, R.; Restrepo, A.; Merino, G. *Phys. Chem. Chem. Phys.* **2015**, *17*, 8769−8775.
(12) Castro, A. S.; Audiffred, M.; Mercero, J. M.; Ugalde, J. M.; Méndez-Rojas, M. A.; Merino, G. *Chem. Phys. Lett.* **2012**, *519*, 29−33.
(13) Cui, Z. H.; Contreras, M.; Ding, Y. H.; Merino, G. *J. Am. Chem. Soc.* **2011**, *133*, 13228−13231.
(14) Wu, Y. B.; Jiang, J. L.; Zhang, R. W.; Wang, Z. X. *Chem. - Eur. J.* **2010**, *16*, 1271−1280.
(15) Wang, Z. X.; Schleyer, P. v. R. *Science* **2001**, *292*, 2465−2469.
(16) Pei, Y.; An, W.; Ito, K.; Schleyer, P. v. R.; Zeng, X. C. *J. Am. Chem. Soc.* **2008**, *130*, 10394−10400.
(17) Jimenez-Halla, J. O. C.; Wu, Y. B.; Wang, Z. X.; Islas, R.; Heine, T.; Merino, G. *Chem. Commun.* **2009**, *46*, 8776−8778.
(18) Grande-Aztatzi, R.; Cabellos, J. L.; Islas, R.; Infante, I.; Mercero, J. M.; Restrepo, A.; Merino, G. *Phys. Chem. Chem. Phys.* **2015**, *17*, 4620−4624.
(19) Castro, A. C.; Martínez-Guajardo, G.; Johnson, T.; Ugalde, J. M.; Wu, Y. B.; Mercero, J. M.; Heine, T.; Donald, K. J.; Merino, G. *Phys. Chem. Chem. Phys.* **2012**, *14*, 14764−14768.
(20) Exner, K.; Schleyer, P. v. R. *Science* **2000**, *290*, 1937−1940.
(21) Pei, Y.; Zeng, X. C. *J. Am. Chem. Soc.* **2008**, *130*, 2580−2592.
(22) Wu, Y. B.; Duan, Y.; Lu, G.; Lu, H. G.; Yang, P.; Schleyer, P. v. R.; Merino, G.; Islas, R.; Wang, Z. X. *Phys. Chem. Chem. Phys.* **2012**, *14*, 14760−14763.
(23) Zhai, H. J.; Alaxandrova, A. N.; Birch, K. A.; Boldyrev, A. I.; Wang, L. S. *Angew. Chem., Int. Ed.* **2003**, *42*, 6004−6008.
(24) Alexandrova, A. N.; Zhai, H. J.; Wang, L. S.; Boldyrev, A. I. *Inorg. Chem.* **2004**, *43*, 3552−3554.
(25) Schleyer, P. v. R.; Boldyrev, A. I. *J. Chem. Soc., Chem. Commun.* **1991**, 1536−1538.
(26) Nayak, S. K.; Rao, B. K.; Jena, P.; Li, X.; Wang, L. S. *Chem. Phys. Lett.* **1999**, *301*, 379−384.
(27) Li, S. D.; Ren, G. M.; Miao, C. Q.; Jin, Z. H. *Angew. Chem., Int. Ed.* **2004**, *43*, 1371−1373.
(28) Zhang, X. M.; Lv, J.; Ji, F.; Wu, H. S.; Jiao, H. J.; Schleyer, P. v. R. *J. Am. Chem. Soc.* **2011**, *133*, 4788−4790.
(29) Li, S. D.; Miao, C. Q.; Guo, J. C.; Ren, G. M. *J. Am. Chem. Soc.* **2004**, *126*, 16227−16231.
(30) Driess, M.; Aust, J.; Merz, K.; von Wüllen, C. *Angew. Chem., Int. Ed.* **1999**, *38*, 3677−3680.
(31) Driess, M.; Ackermann, H.; Aust, J.; Merz, K.; von Wüllen, C. *Angew. Chem., Int. Ed.* **2002**, *41*, 450−453.
(32) Romanescu, C.; Galeev, T. R.; Li, W. L.; Boldyrev, A. I.; Wang, L. S. *Acc. Chem. Res.* **2013**, *46*, 350−358.
(33) Ito, K.; Pu, Z. F.; Li, Q. S.; Schleyer, P. v. R. *Inorg. Chem.* **2008**, *47*, 10906−10910.
(34) Pu, Z. F.; Ito, K.; Schleyer, P. v. R.; Li, Q. S. *Inorg. Chem.* **2009**, *48*, 10679−10686.
(35) Romanescu, C.; Galeev, T. R.; Sergeeva, A. P.; Li, W. L.; Wang, L. S.; Boldyrev, A. I. *J. Organomet. Chem.* **2012**, *154*, 721−722.
(36) Romanescu, C.; Galeev, T. R.; Li, W. L.; Boldyrev, A. I.; Wang, L. S. *Angew. Chem., Int. Ed.* **2011**, *50*, 9334−9337.
(37) Li, W. L.; Romanescu, C.; Galeev, T. R.; Piazza, Z. A.; Boldyrev, A. I.; Wang, L. S. *J. Am. Chem. Soc.* **2012**, *134*, 165−168.
(38) Romanescu, C.; Galeev, T. R.; Li, W. L.; Boldyrev, A. I.; Wang, L. S. *J. Chem. Phys.* **2013**, *138*, 134315.
(39) Galeev, T. R.; Romanescu, C.; Li, W. L.; Wang, L. S.; Boldyrev, A. I. *Angew. Chem., Int. Ed.* **2012**, *51*, 2101−2105.
(40) Heine, T.; Merino, G. *Angew. Chem., Int. Ed.* **2012**, *51*, 4275−4276.
(41) Pancharatna, P. D.; Méndez-Rojas, M. A.; Merino, G.; Vela, A.; Hoffmann, R. *J. Am. Chem. Soc.* **2004**, *126*, 15309−15315.
(42) Luo, X. Y.; Yang, J. H.; Liu, H. Y.; Wu, X. J.; Wang, Y. C.; Ma, Y. M.; Wei, S. H.; Gong, X. G.; Xiang, H. J. *J. Am. Chem. Soc.* **2011**, *133*, 16285−16290.
(43) Zhang, Z. H.; Liu, X. F.; Yakobson, B. I.; Guo, W. L. *J. Am. Chem. Soc.* **2012**, *134*, 19326−19329.
(44) Dai, J.; Wu, X. J.; Yang, J. L.; Zeng, X. C. *J. Phys. Chem. Lett.* **2014**, *5*, 2058−2065.
(45) Li, Y. F.; Liao, Y. L.; Schleyer, P. v. R.; Chen, Z. *Nanoscale* **2014**, *6*, 10784−10791.
(46) Li, Y. F.; Liao, Y. L.; Chen, Z. *Angew. Chem., Int. Ed.* **2014**, *53*, 7248−7252.
(47) (a) Li, Y. F.; Li, F. Y.; Zhou, Z.; Chen, Z. *J. Am. Chem. Soc.* **2011**, *133*, 900−908. (b) Yang, L. M.; Popov, I. A.; Boldyrev, A. I.; Heine, T.; Frauenheim, T.; Ganz, E. *Phys. Chem. Chem. Phys.* **2015**, *17*, 17545−17551. (c) Yang, L. M.; Popov, I. A.; Frauenheim, T.; Boldyrev, A. I.; Heine, T.; Bačić, V.; Ganz, E. *Phys. Chem. Chem. Phys.* **2015**, *17*,

DOI: 10.1021/jacs.6b01769
J. Am. Chem. Soc. 2016, 138, 5644−5651

26043−26048. (d) Yang, L. M.; Bačić, V.; Popov, I. A.; Boldyrev, A. I.; Heine, T.; Frauenheim, T.; Ganz, E. *J. Am. Chem. Soc.* **2015**, *137*, 2757−2762.
(48) (a) Yang, L. M.; Frauenheim, T.; Ganz, E. *Phys. Chem. Chem. Phys.* **2015**, *17*, 19695−19699. (b) Yang, L. M.; Dornfeld, M.; Frauenheim, T.; Ganz, E. *Phys. Chem. Chem. Phys.* **2015**, *17*, 26036−26042. (c) Yang, L. M.; Ganz, A. B.; Dornfeld, M.; Ganz, E. *Condens. Matter* **2016**, DOI: 10.3390/condmat1010001.
(49) Hou, J. H.; Duan, Q.; Qin, J. M.; Shen, X. D.; Zhao, J. X.; Liang, Q. C.; Jiang, D. Y.; Gao, S. *Phys. Chem. Chem. Phys.* **2015**, *17*, 9644−9650.
(50) Kresse, G.; Hafner, J. *Phys. Rev. B: Condens. Matter Mater. Phys.* **1993**, *48*, 13115−13118.
(51) Kresse, G.; Furthmuller, J. *Phys. Rev. B: Condens. Matter Mater. Phys.* **1996**, *54*, 11169−11186.
(52) Kresse, G.; Joubert, D. *Phys. Rev. B: Condens. Matter Mater. Phys.* **1999**, *59*, 1758−1775.
(53) Perdew, J. P.; Burke, K.; Ernzerhof, M. *Phys. Rev. Lett.* **1996**, *77*, 3865−3868.
(54) Togo, A.; Oba, F.; Tanaka, I. *Phys. Rev. B: Condens. Matter Mater. Phys.* **2008**, *78*, 134106.
(55) Gonze, X.; Lee, C. *Phys. Rev. B: Condens. Matter Mater. Phys.* **1997**, *55*, 10355−10368.
(56) Martyna, G. J.; Klein, M. L.; Tuckerman, M. *J. Chem. Phys.* **1992**, *97*, 2635−2643.
(57) Wang, Y. C.; Lv, J.; Zhu, L.; Ma, Y. M. *Phys. Rev. B: Condens. Matter Mater. Phys.* **2010**, *82*, 094116.
(58) Luo, X.; Yang, J.; Liu, H.; Wu, X. J.; Wang, Y. C.; Ma, Y. M.; Wei, S. H.; Gong, X. G.; Xiang, H. J. *J. Am. Chem. Soc.* **2011**, *133*, 16285−16290.
(59) Wu, X. J.; Dai, J.; Zhao, Y.; Zhuo, Z.; Yang, J. L.; Zeng, X. C. *ACS Nano* **2012**, *6*, 7443−7453.
(60) (a) Yu, X.; Li, L.; Xu, X. W.; Tang, C. C. *J. Phys. Chem. C* **2012**, *116*, 20075−20079. (b) Ma, F. X.; Jiao, Y. L.; Gao, G. P.; Gu, Y. T.; Bilic, A.; Chen, Z. F.; Du, A. J. *Nano Lett.* **2016**, DOI: 10.1021/acs.nanolett.5b05292.
(61) Heyd, J.; Scuseria, G. E.; Ernzerhof, M. *J. Chem. Phys.* **2003**, *118*, 8207−8215.
(62) Zhang, H. J.; Wu, D. H.; Tang, Q.; Liu, L.; Zhou, Z. *J. Mater. Chem. A* **2013**, *1*, 2231−2237.
(63) Saha, S.; Sinha, T. P.; Mookerjee, A. *Phys. Rev. B: Condens. Matter Mater. Phys.* **2000**, *62*, 8828.
(64) Gajdoš, M.; Hummer, K.; Kresse, G.; Furthmüller, J.; Bechstedt, F. *Phys. Rev. B: Condens. Matter Mater. Phys.* **2006**, *73*, 045112.
(65) Molina-Sánchez, A.; Wirtz, L. *Phys. Rev. B: Condens. Matter Mater. Phys.* **2011**, *84*, 155413.
(66) Martínez-Guajardo, G.; Cabell, K.; Heine, T.; Merino, G. *Sci. Rep.* **2015**, *5*, 11287.
(67) Reckien, W.; Jantzko, F.; Peintinger, M.; Bredow, T. *J. Comput. Chem.* **2012**, *33*, 2023.
(68) Wyckoff, R. W. G. *Crystal Structures*, 2nd ed.; Interscience Publishers: New York, 1963; Vol. *1*, pp 7−83.
(69) Zhong, X. L.; Yap, Y. K.; Pandey, R. *Phys. Rev. B: Condens. Matter Mater. Phys.* **2011**, *83*, 193403.
(70) Savin, A.; Nesper, R.; Wengert, S.; Fässler, T. F. *Angew. Chem., Int. Ed. Engl.* **1997**, *36*, 1808−1832.
(71) Zhang, S. H.; Wang, Q.; Kawazoe, Y.; Jena, P. *J. Am. Chem. Soc.* **2013**, *135*, 18216−18221.
(72) Galeev, T. R.; Dunnington, B. D.; Schmidt, J. R.; Boldyrev, A. I. *Phys. Chem. Chem. Phys.* **2013**, *15*, 5022−5029.
(73) Zhang, H. J.; Liu, L.; Zhou, Z. *Phys. Chem. Chem. Phys.* **2012**, *14*, 1286−1292.
(74) Zhang, H. J.; Liu, L.; Zhou, Z. *RSC Adv.* **2012**, *2*, 9224−9229.
(75) Liu, H. S.; Gao, J. F.; Zhao, J. J. *Sci. Rep.* **2013**, *3*, 3238.
(76) Zhang, Z.; Yang, Y.; Gao, G.; Yakobson, B. I. *Angew. Chem., Int. Ed.* **2015**, *54*, 13022−13026.
(77) Mannix, A. J.; Zhou, X.; Kiraly, B.; Wood, J. D.; Alducin, D.; Myers, B. D.; Liu, X.; Fisher, B. L.; Santiago, U.; Guest, J. R.; Yacaman, M. J.; Ponce, A.; Oganov, A. R.; Hersam, M. C.; Guisinger, N. P. *Science* **2015**, *350*, 1513−1516.

DOI: 10.1021/jacs.6b01769
J. Am. Chem. Soc. 2016, 138, 5644−5651